

Can Zee-Babu model implemented with scalar dark matter explain both Fermi-LAT 130 GeV γ -ray excess and neutrino physics ?

Seungwon Baek^a P. Ko,^a Hiroshi Okada,^a and Eibun Senaha^{a,b}

^a*School of Physics, KIAS, Seoul 130-722, Korea*

^b*Department of Physics, Nagoya University, Nagoya 464-8602, Japan*

E-mail: swbaek@kias.re.kr, pko@kias.re.kr, hokada@kias.re.kr,
senaha@kias.re.kr

ABSTRACT: We extend the Zee-Babu model for the neutrino masses and mixings by first incorporating a scalar dark matter X with Z_2 symmetry and then X and a dark scalar φ with global $U(1)$ symmetry. In the latter scenario the singly and doubly charged scalars that are new in the Zee-Babu model can explain the large annihilation cross section of a dark matter pair into two photons as hinted by the recent analysis of the Fermi γ -ray space telescope data. These new scalars can also enhance the $B(H \rightarrow \gamma\gamma)$, as the recent LHC results may suggest. The dark matter relic density can be explained. The direct detection rate of the dark matter is predicted to be about one order of magnitude down from the current experimental bound in the first scenario.

KEYWORDS:

Contents

1	Introduction	1
2	The Z_2 model	3
2.1	Constraints on the potential	3
2.2	$XX \rightarrow \gamma\gamma$ and Fermi-LAT 130 GeV γ -ray excess	5
2.3	Thermal relic density and direct detection rate	7
2.4	$H \rightarrow \gamma\gamma$	8
2.5	Implications for neutrino physics	9
3	Spontaneously broken $U(1)_{B-L}$ model	10
3.1	$X_R X_R \rightarrow \gamma\gamma$ and Fermi-LAT 130 GeV γ -ray excess in $U(1)_{B-L}$ model	12
3.2	Relic density in $U(1)_{B-L}$ model	14
4	Conclusions	18
A	One-loop β functions of the quartic couplings	19
B	The annihilation cross section of $X_R X_R \rightarrow \alpha\alpha$	20

1 Introduction

Although it is well known that the dark matter (DM) constitutes about 27% of the total mass density of the universe, *i.e.* $\Omega_{\text{DM}} h^2 = 0.1199 \pm 0.0027$ [1], its existence has only been inferred from the gravitational interaction. And its nature is still unknown. If the DM is weakly interacting massive particle (WIMP), it may reveal itself via non-gravitational interactions, for example, by pair annihilation into ordinary standard model (SM) particles including photon [2]. In this case, the DM relic abundance is roughly related to the pair annihilation cross section at freezeout, $\langle\sigma v\rangle_{\text{th}}$, as

$$\Omega_{\text{DM}} h^2 = \frac{3 \times 10^{-27} \text{cm}^3/\text{s}}{\langle\sigma v\rangle_{\text{th}}}. \quad (1.1)$$

Recently Refs. [3, 4] claim that the Fermi γ -ray space telescope may have seen excess of the photons with $E_\gamma \sim 130$ GeV from the center of the Milky Way compared with the background. Interpreting its origin as the annihilation of a pair of DM particles, they could obtain the annihilation cross section to be about 4% of that at freezeout:

$$\langle\sigma v\rangle_{\gamma\gamma} \approx 0.04 \langle\sigma v\rangle_{\text{th}} \approx 0.04 \text{ pb} \approx 1.2 \times 10^{-27} \text{cm}^3/\text{s}. \quad (1.2)$$

Since DM is electrically neutral, the pair annihilation process into photons occurs through loop-induced diagrams. Naively we expect

$$\frac{\langle\sigma v\rangle_{\gamma\gamma}}{\langle\sigma v\rangle_{\text{th}}} = \left(\frac{\alpha_{\text{em}}}{\pi}\right)^2 \sim 10^{-5}. \quad (1.3)$$

So the observed value in (1.2) is rather large, and we may need new electrically charged particles running inside the loop beyond the SM. Many new physics scenarios were speculated within various CDM models by this observation [5].

The so-called ‘Zee-Babu model’ [7–9] provides new charged scalars, h^+, k^{++} at electroweak scale, in addition to the SM particles. These new charged scalars carry two units of lepton number and can generate Majorana neutrino masses via two-loop diagrams. The diagrams are finite and calculable. The neutrino masses are naturally small without the need to introduce the right-handed neutrinos for seesaw mechanism. One of the neutrinos is predicted to be massless in this model. Both normal and inverse hierarchical pattern of neutrino masses are allowed. The observed mixing pattern can also be accommodated. The model parameters are strongly constrained by the neutrino mass and mixing data, the radiative muon decay, $\mu \rightarrow e\gamma$, and $\tau \rightarrow 3\mu$ decay [10].

It would be very interesting to see if the new charged particles in the Zee-Babu model can participate in some other processes in a sector independent of neutrinos. In the first part of this paper, we minimally extend the Zee-Babu model to incorporate the DM. In the later part we will consider more extended model with global $U(1)_{B-L}$ symmetry and an additional scalar which breaks the global symmetry [12].

In the first scenario, we introduce a real scalar dark matter X with a discrete Z_2 symmetry under which the dark matter transforms as $X \rightarrow -X$ in order to guarantee its stability. The renormalizable interactions between the scalar DM X with the Higgs field and the Zee-Babu scalar fields provide a Higgs portal between the SM sector and the DM. We show that the Zee-Babu scalars and their interactions with the DM particle can explain the DM relic density. The branching ratio of Higgs to two photons, $B(H \rightarrow \gamma\gamma)$, can also be enhanced as implied by the recent LHC results [15]. The spin-independent cross section of the dark matter scattering off the proton, σ_p , is less than about 1×10^{-9} pb, which can be probed at next generation searches. Although the charged Zee-Babu scalars enhance the $XX \rightarrow \gamma\gamma$ process, it turns out the the current experimental constraints on their masses do not allow the annihilation cross section to reach (1.2).

In the extended scenario, we consider a complex scalar dark matter X and a dark scalar φ [12]. The global $U(1)$ symmetry of the original Lagrangian is broken down to Z_2 by φ getting a vacuum expectation value (vev). We show that both the dark matter relic abundance and the Fermi-LAT gamma-ray line signal can be accommodated via two mechanisms.

This paper is organized as follows. In Section 2, we define our model by including the scalar DM in the Zee-Babu model, and consider theoretical constraints on the scalar potential. Then we study various DM phenomenology. We calculate the dark matter relic density and the annihilation cross section $\langle\sigma v\rangle_{\gamma\gamma}$ in our model. We also predict the cross section for the DM and proton scattering and the branching ratio for the Higgs decay into

two photons, $B(H \rightarrow \gamma\gamma)$. And we consider the implication on the neutrino sector. In Section 3, we consider the DM phenomenology in the extended model. We conclude in Section 4.

2 The Z_2 model

We implement the Zee-Babu model for radiative generation of neutrino masses and mixings, by including a real scalar DM X with Z_2 symmetry $X \rightarrow -X$. All the possible renormalizable interactions involving the scalar fields are given by

$$\mathcal{L} = \mathcal{L}_{\text{Babu}} + \mathcal{L}_{\text{Higgs+DM}} \quad (2.1)$$

$$\mathcal{L}_{\text{Babu}} = f_{ab} l_{aL}^{Ti} C l_{bL}^j \epsilon_{ij} h^+ + h'_{ab} l_{aR}^T C l_{bR} k^{++} + h.c. \quad (2.2)$$

$$\begin{aligned} -\mathcal{L}_{\text{Higgs+DM}} = & -\mu_H^2 H^\dagger H + \frac{1}{2} \mu_X^2 X^2 + \mu_h^2 h^+ h^- + \mu_k^2 k^{++} k^{--} \\ & + (\mu_{hk} h^- h^- k^{++} + h.c.) \\ & + \lambda_H (H^\dagger H)^2 + \frac{1}{4} \lambda_X X^4 + \lambda_h (h^+ h^-)^2 + \lambda_k (k^{++} k^{--})^2 \\ & + \frac{1}{2} \lambda_{HX} H^\dagger H X^2 + \lambda_{Hh} H^\dagger H h^+ h^- + \lambda_{Hk} H^\dagger H k^{++} k^{--} \\ & + \frac{1}{2} \lambda_{Xh} X^2 h^+ h^- + \frac{1}{2} \lambda_{Xk} X^2 k^{++} k^{--} + \lambda_{hk} h^+ h^- k^{++} k^{--}. \end{aligned} \quad (2.3)$$

Note that our model is similar to the model proposed by J. Cline [6]. However we included the interaction between the new charged scalar and the SM leptons that are allowed by gauge symmetry, and thus the new charged scalar bosons are not stable and cause no problem.

The original Zee-Babu model was focused on the neutrino physics, and the operators of Higgs portal types were not discussed properly. It is clear that those Higgs portal operators we include in the 2nd line of (2.3) can enhance $H \rightarrow \gamma\gamma$, without touching any other decay rates of the SM Higgs boson, as long as h^\pm and $k^{\pm\pm}$ are heavy enough that the SM Higgs decays into these new scalar bosons are kinematically forbidden.

2.1 Constraints on the potential

We require μ_X^2 , μ_h^2 and μ_k^2 to be positive. Otherwise the imposed Z_2 symmetry $X \rightarrow -X$ or the electromagnetic $U(1)$ symmetry could be spontaneously broken down. Since the masses of X , k^{++} and h^+ have contributions from the electroweak symmetry breaking as

$$\begin{aligned} m_X^2 &= \mu_X^2 + \frac{1}{2} \lambda_{HX} v_H^2, \\ m_{h^+}^2 &= \mu_h^2 + \frac{1}{2} \lambda_{Hh} v_H^2, \\ m_{k^{++}}^2 &= \mu_k^2 + \frac{1}{2} \lambda_{Hk} v_H^2, \end{aligned} \quad (2.4)$$

we obtain the conditions on the quartic couplings

$$\lambda_{HX} < \frac{2m_X^2}{v_H^2}, \quad \lambda_{Hh} < \frac{2m_{h^+}^2}{v_H^2}, \quad \lambda_{Hk} < \frac{2m_{k^{++}}^2}{v_H^2}. \quad (2.5)$$

We note that the above conditions are automatically satisfied if the couplings takes negative values. In such a case, however, we also need to worry about the behavior of the Higgs potential for large field values. For example, if we consider only the neutral Higgs field, H^1 , and the dark matter field, X , we get

$$\begin{aligned} V &\sim \frac{1}{4}\lambda_H H^4 + \frac{1}{4}\lambda_X X^4 + \frac{1}{4}\lambda_{HX} H^2 X^2, \\ &\sim \frac{1}{4} \begin{pmatrix} H^2 & X^2 \end{pmatrix} \begin{pmatrix} \lambda_H & \frac{1}{2}\lambda_{HX} \\ \frac{1}{2}\lambda_{HX} & \lambda_X \end{pmatrix} \begin{pmatrix} H^2 \\ X^2 \end{pmatrix}, \end{aligned} \quad (2.6)$$

for large field values of H and X . If the potential is to be bounded from below, every eigenvalue of the square matrix of the couplings in (2.6) should be positive, whose condition is

$$|\lambda_{HX}| < \sqrt{4\lambda_H\lambda_X}. \quad (2.7)$$

This means that even if λ_{HX} is negative, its absolute value should not be arbitrarily large because $\lambda_H = m_H^2/2v_H^2 \approx 0.13$ ($m_H \approx 125$ GeV) and λ_X is bounded from above so as not to generate the Landau pole. For example, the renormalization group running equations (RGEs) of λ_H , λ_X and λ_{HX} are given by

$$\begin{aligned} \frac{d\lambda_H}{d\log Q} &= \frac{1}{16\pi^2} \left(24\lambda_H^2 + \frac{1}{2}\lambda_{HX}^2 \right) + \dots, \\ \frac{d\lambda_X}{d\log Q} &= \frac{1}{16\pi^2} \left(18\lambda_X^2 + 2\lambda_{HX}^2 \right) + \dots, \\ \frac{d\lambda_{HX}}{d\log Q} &= \frac{\lambda_{HX}}{8\pi^2} \left(6\lambda_H + 3\lambda_X \right) + \dots, \end{aligned} \quad (2.8)$$

where the dots represents other contributions which are not important in the discussion. The complete forms of the β -functions of the quartic couplings are listed in Appendix A.

The approximate solution for λ_X in (2.8) shows that the Landau pole is generated at the scale $Q = Q_{EW} \exp(1/\beta_H \lambda_X(Q_{EW}))$ ($\beta_H = 18/16\pi^2$). If we take the electroweak scale value of the Higgs quartic coupling to be $\lambda_X(Q_{EW}) \sim 5$, the cut-off scale should be around 1 TeV. The general condition for the bounded-from-below potential for large field values is that all the eigenvalues of the matrix

$$\begin{pmatrix} \lambda_H & \frac{1}{2}\lambda_{HX} & \lambda_{Hh} & \lambda_{Hk} \\ \frac{1}{2}\lambda_{HX} & \lambda_X & \lambda_{Xh} & \lambda_{Xk} \\ \lambda_{Hh} & \lambda_{Xh} & 4\lambda_h & 2\lambda_{hk} \\ \lambda_{Hk} & \lambda_{Xk} & 2\lambda_{hk} & 4\lambda_k \end{pmatrix} \quad (2.9)$$

should be positive.

In the following discussion, we require that all scalar quartic couplings (λ_i) be perturbative up to some scale Q . To this end, we solve the one-loop RGEs of those quartic couplings given in Appendix A. For the moment, we do not include new Yukawa couplings

¹We use the same notation with the Higgs doublet.

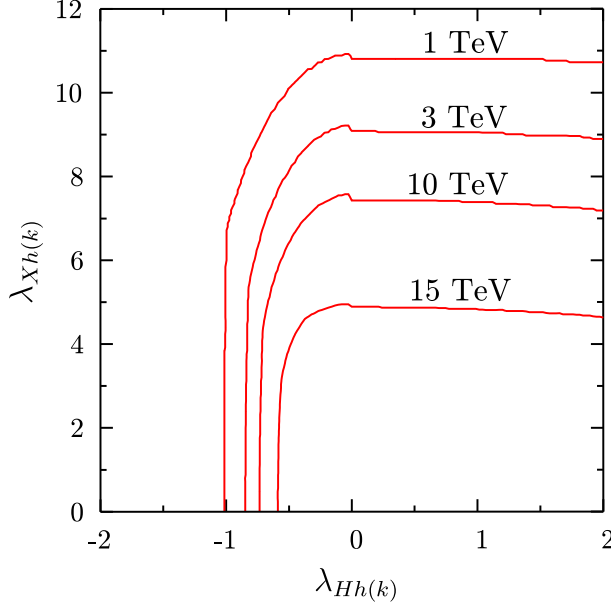


Figure 1. The perturbativity bounds, $\lambda_i(Q) < 4\pi$ are shown. The each curve denotes $Q = 1, 3, 10$ and 15 TeV from top to bottom. We take $\lambda_{Hh} = \lambda_{Hk}$, $\lambda_{Xh} = \lambda_{Xk}$, $\lambda_{hk} = \lambda_{HX} = 0$ and $\lambda_X = \lambda_H (\simeq 0.13)$. For the negative λ_{Hk} , we set $\lambda_h = \lambda_{Hh}^2/(2\lambda_H)$ and $\lambda_k = \lambda_{Hk}^2/(2\lambda_H)$ while $\lambda_h = \lambda_k = \lambda_H$ for positive λ_{Hk} .

defined in Eq. (2.2), and we adopt the criterion $\lambda_i(Q) < 4\pi$ in this analysis. In Fig. 1, the perturbativity bounds are shown in the $\lambda_{Xh(k)}\text{-}\lambda_{Hh(k)}$ plane. We take $Q = 1, 3, 10$ and 15 TeV, which are denoted by the red curves from top to bottom. For other parameters, we fix $\lambda_{Hh} = \lambda_{Hk}$, $\lambda_{Xh} = \lambda_{Xk}$, $\lambda_{hk} = \lambda_{HX} = 0$ and $\lambda_X = \lambda_H (\simeq 0.13)$. As explained above, a certain negative value of $\lambda_{Hk(h)}$ may cause the instability of the Higgs potential. To avoid this, we set $\lambda_h = \lambda_{Hh}^2/(2\lambda_H)$ and $\lambda_k = \lambda_{Hk}^2/(2\lambda_H)$ for $\lambda_{Hk(h)} < 0$. For $\lambda_{Hk(h)} > 0$, on the other hand, $\lambda_h = \lambda_k = \lambda_H$ is taken. As we see from the plot, $\lambda_{Xk(h)} \simeq 7 - 11$ is possible if $Q = 1$ TeV.

The theoretical arguments (2.5) and (2.7) restrict λ_{HX} to lie roughly to the range, $(-1.6, 0.6)$. Similarly, we have $\lambda_{Hh(k)} \lesssim 0.7$ for $m_{h+(k++)} = 150$ GeV.

2.2 $XX \rightarrow \gamma\gamma$ and Fermi-LAT 130 GeV γ -ray excess

The annihilation cross section for $XX \rightarrow \gamma\gamma$ is given by

$$\langle\sigma v\rangle_{\gamma\gamma} = \frac{\sum |\mathcal{M}|^2}{64\pi m_X^2}, \quad (2.10)$$

where the amplitude-squared summed over the photon polarization is

$$\begin{aligned} \sum |\mathcal{M}|^2 &= \frac{\alpha_{\text{em}}^2}{2\pi^2} \left| \lambda_{Xh} A_0(\tau_{h+}) + 4\lambda_{Xk} A_0(\tau_{k++}) \right. \\ &\quad \left. + \frac{\lambda_{HX} v_H^2}{s - m_H^2 + im_H \Gamma_H} \left[\frac{g^2}{2\tau_W} \left(Q_t^2 N_C A_{1/2}(\tau_t) + A_1(\tau_W) \right) \right] \right|^2 \end{aligned}$$

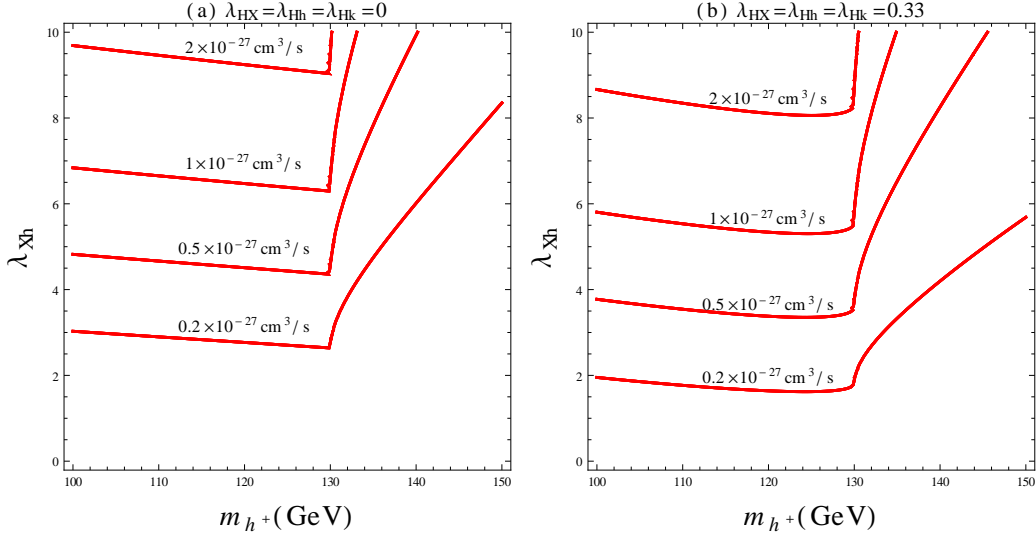


Figure 2. Contour plot of $\langle\sigma v\rangle_{\gamma\gamma} = (2, 1, 0.5, 0.2) \times 10^{-27} \text{ cm}^3/\text{s}$ (from above) in (m_{h^+}, λ_{Xh}) plane. We set $m_X = 130$ GeV, $m_H = 125$ GeV, $m_k = 500$ GeV and $\lambda_{Xk} = 5$, $\lambda_{HX} = \lambda_{Hh} = \lambda_{Hk} = 0(0.33)$ in the left (right) panel.

$$+ \lambda_{Hh} A_0(\tau_{h^+}) + 4\lambda_{Hk} A_0(\tau_{k^{++}}) \Bigg]^2, \quad (2.11)$$

with $\tau_i = 4m_i^2/s$ ($i = h^+, k^{++}, t, W$). The loop functions are

$$\begin{aligned} A_0(\tau) &= 1 - \tau f(\tau), \\ A_{1/2}(\tau) &= -2\tau \left[1 + (1 - \tau)f(\tau) \right], \\ A_1(\tau) &= 2 + 3\tau + 3\tau(2 - \tau)f(\tau), \end{aligned} \quad (2.12)$$

where

$$f(\tau) = \begin{cases} \arcsin^2 \sqrt{1/\tau}, & (\tau \geq 1) \\ -\frac{1}{4} \left[\log \frac{1+\sqrt{1-\tau}}{1-\sqrt{1-\tau}} - i\pi \right]^2, & (\tau < 1). \end{cases} \quad (2.13)$$

Although the contribution of the doubly-charged Higgs k^{++} to $\langle\sigma v\rangle_{\gamma\gamma}$ is $2^4 = 16$ times larger than that of the singly-charged Higgs h^+ when their masses are similar to each other, this option is ruled out by the recent LHC searches for the doubly-charged Higgs boson [16]. Depending on the decay channels, the 95% CL lower limit on the mass of the doubly-charged Higgs boson is in the range, 204–459 GeV. To be conservative, we set $m_{k^{++}} = 500$ GeV. In Figure 2, we show a contour plot for the annihilation cross section into two photons: $\langle\sigma v\rangle_{\gamma\gamma} \approx (2, 1, 0.5, 0.2) \times 10^{-27} \text{ cm}^3/\text{s}$ (from above) in the (m_{h^+}, λ_{Xh}) plane. We set $m_X = 130$ GeV, $m_H = 125$ GeV, $m_{k^{++}} = 500$ GeV and $\lambda_{Xk} = 5$, $\lambda_{HX} = \lambda_{Hh} = \lambda_{Hk} = 0$ (0.33) in the left (right) panel. We can see that by turning on the process, $XX \rightarrow H \rightarrow \gamma\gamma$, with $\lambda_{HX} = 0.33$ (right panel), we can reduce λ_{Xh} to get $\langle\sigma v\rangle_{\gamma\gamma} = 1 \times 10^{-27} \text{ cm}^3/\text{s}$ to explain the Fermi-LAT gamma-ray line signal, but not significantly enough to push the cut-off

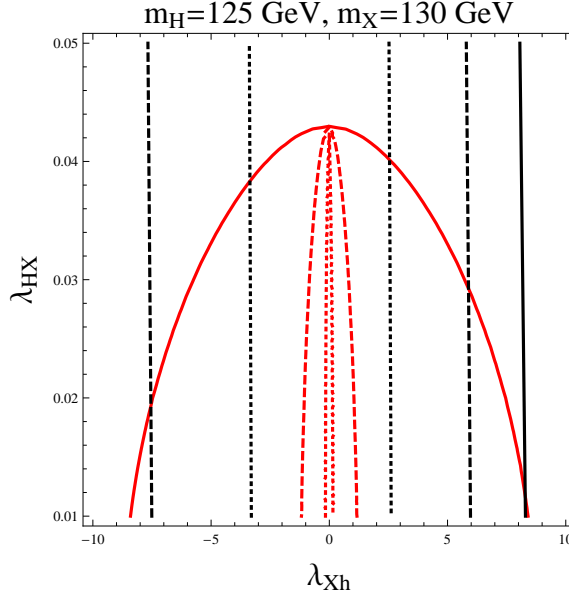


Figure 3. The contour plot of $\Omega_{\text{DM}} h^2 = 0.1199$ (red lines) and $\langle \sigma v \rangle_{\gamma\gamma} = 0.2 \times 10^{-27} \text{cm}^3/\text{s}$ (black lines) in the $(\lambda_{Xh}, \lambda_{HX})$ plane for the choices $m_{h^+} = 150, 140, 130$ GeV (solid, dashed, dotted lines). For other parameters we set $m_X = 130$ GeV, $m_H = 125$ GeV, $m_k = 500$ GeV, $\lambda_{Xk} = 5$, $\lambda_{Hh} = \lambda_{Hk} = 0.5$.

scale much higher than the electroweak scale. As we will see in the following section, the $\langle \sigma v \rangle_{\gamma\gamma} = 1 \times 10^{-27} \text{cm}^3/\text{s}$ is not consistent with the current DM relic abundance.

2.3 Thermal relic density and direct detection rate

Contrary to J. Cline’s model [6], the DM relic density in our model is not necessarily correlated with the $\langle \sigma v \rangle_{\gamma\gamma}$, since it is mainly determined by λ_{HX} for relatively heavy scalars ($\gtrsim 150$ GeV). In this case the main DM annihilation channels are $XX \rightarrow H \rightarrow \text{SM particles}$, where the SM particles are W^+W^- , ZZ , $b\bar{b}$, *etc.* As $m_{h^+(k^{++})}$ becomes comparable with m_X , the $XX \rightarrow h^+h^-(k^{++}k^{--})$ modes can open, even in cases $m_X < m_{h^+}(m_{k^{++}})$ due to the kinetic energy of X at freeze-out time. This can be seen in Figure 3, where we show the contour plot of $\Omega_{\text{DM}} h^2 = 0.1199$ (red lines) in the $(\lambda_{Xh}, \lambda_{HX})$ plane for the choices $m_{h^+} = 150, 140, 130$ GeV (shown in solid, dashed, dotted lines respectively). We fixed other parameters to be $m_X = 130$ GeV, $m_H = 125$ GeV, $m_k = 500$ GeV, $\lambda_{Xk} = 5$, $\lambda_{Hh} = \lambda_{Hk} = 0.5$. For $m_{h^+} = 130$ GeV, the annihilation mode $XX \rightarrow h^+h^-$ dominates even for very small coupling λ_{Xh} (the red dotted line). The black vertical lines are the constant contour lines of $\langle \sigma v \rangle_{\gamma\gamma} = 0.2 \times 10^{-27} \text{cm}^3/\text{s}$. We can see that the maximum value for the Fermi-LAT gamma-ray line signal which is consistent with the relic density is $\langle \sigma v \rangle_{\gamma\gamma} = 0.2 \times 10^{-27} \text{cm}^3/\text{s}$ when $m_{h^+} = 150$ GeV. This cross section is smaller than the required value in (1.2) by factor 6.

Figure 4 shows the cross section of dark matter scattering off proton, σ_p , as a function of λ_{HX} (red solid line) and $\sigma_p = 1.8 \times 10^{-9}$ pb line (black dashed line) above which is excluded by LUX [17] at 90% C.L. This cross section is determined basically only by λ_{HX}

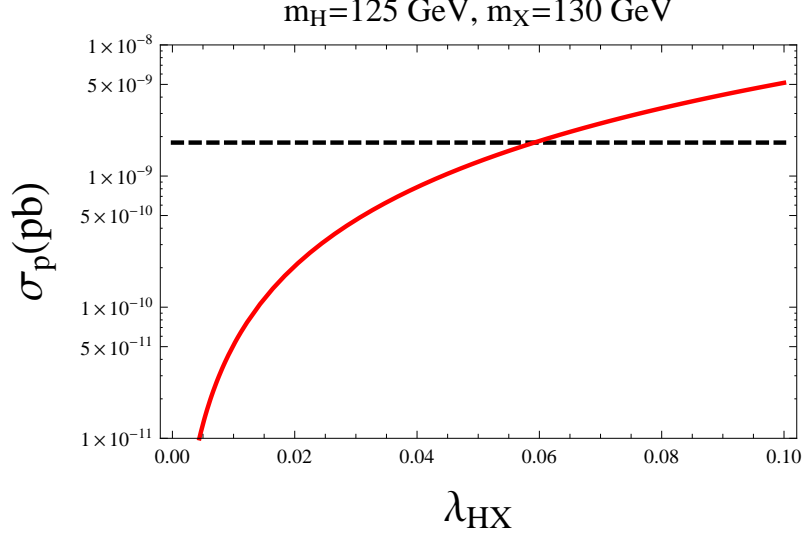


Figure 4. The spin-independent cross section of dark matter scattering off proton, σ_p , as a function of λ_{HX} (red solid line) and $\sigma_p = 1.8 \times 10^{-9}$ pb line above which is excluded by LUX (black dashed line). We take $m_H = 125$ GeV and $m_X = 130$ GeV.

at tree level by the SM Higgs exchange, when we fix $m_X = 130$ GeV. We can see that $\lambda_{HX} \lesssim 0.06$ to satisfy the LUX upper bound.

2.4 $H \rightarrow \gamma\gamma$

In this scenario the decay width of $H \rightarrow \gamma\gamma$ is modified, whereas other Higgs decay widths are intact:

$$\begin{aligned} \Gamma(H \rightarrow \gamma\gamma) = & \frac{\alpha_{\text{em}}^2 v_H^2}{64\pi^3 m_H} \left| \lambda_{Hh} A_0(\tau_{h+}) + 4\lambda_{Hk} A_0(\tau_{k++}) \right. \\ & \left. + \frac{g^2}{2\tau_W} \left[A_1(\tau_W) + \sum_{f=t,b} Q_f^2 N_c^f A_{1/2}(\tau_f) \right] \right|^2, \end{aligned} \quad (2.14)$$

where $\tau_i = 4m_i^2/m_H^2$ ($i = f, W, h^+, k^{++}$).

In Figure 5, we show contour plots for constant $\Gamma(H \rightarrow \gamma\gamma)/\Gamma(H \rightarrow \gamma\gamma)^{\text{SM}}$ (black solid lines) and $\Gamma(H \rightarrow Z\gamma)/\Gamma(H \rightarrow Z\gamma)^{\text{SM}}$ (black dashed lines) in the $(\lambda_{Hh}, \lambda_{Hk})$ plane. For this plot we set $m_{h^+} = 130$ (150) GeV for the left (right) panel and fixed $m_{k^{++}} = 500$ GeV. The shaded regions are disfavored by (2.5) (blue) and by (2.7) (yellow). The ratios depend basically only on the coupling constants λ_{Hh} and λ_{Hk} as well as the masses m_{h^+} and $m_{k^{++}}$. And the ratios are not necessarily correlated with the $\langle\sigma v\rangle_{\gamma\gamma}$ which are controlled by λ_{Xh} and λ_{Xk} . We can conclude that

$$\begin{aligned} 0.54 & \lesssim \Gamma(H \rightarrow \gamma\gamma)/\Gamma(H \rightarrow \gamma\gamma)^{\text{SM}} \lesssim 1.45 \quad (1.35) \\ 0.91 & \lesssim \Gamma(H \rightarrow Z\gamma)/\Gamma(H \rightarrow Z\gamma)^{\text{SM}} \lesssim 1.11 \quad (1.08) \end{aligned}$$

for the left (right) panel. That is, the $H \rightarrow \gamma\gamma$ channel can be enhanced (reduced) significantly, whereas the $H \rightarrow Z\gamma$ channel can change only upto $\sim 10\%$.

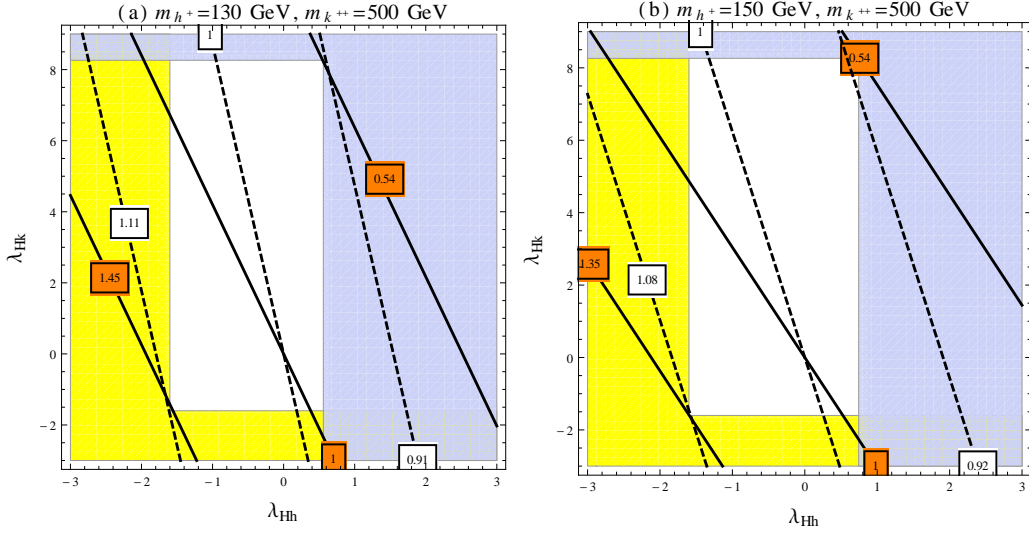


Figure 5. A contour plot for constant $\Gamma(H \rightarrow \gamma\gamma)/\Gamma(H \rightarrow \gamma\gamma)^{\text{SM}}$ (black solid lines) and $\Gamma(H \rightarrow Z\gamma)/\Gamma(H \rightarrow Z\gamma)^{\text{SM}}$ (black dashed lines) in the $(\lambda_{Hh}, \lambda_{Hk})$ plane. The shaded regions are disfavored by (2.5) (blue) and by (2.7) (yellow). We set $m_{h^+} = 130$ (150) GeV for the left (right) panel and fixed $m_{k^{++}} = 500$ GeV.

2.5 Implications for neutrino physics

So far, we did not consider the constraints from neutrino sector and charged lepton flavor violation. In fact, these constraints are rather severe, if we assume that the observed neutrino masses and mixings are entirely from the Zee-Babu mechanism. One cannot afford light h^\pm or $k^{\pm\pm}$, because of the constraints from charged LFV: $m_{h^+} \gtrsim 240$ GeV from $B(\mu \rightarrow e\gamma) < 2.4 \times 10^{-12}$ [18] and $m_{k^{++}} \gtrsim 770$ GeV from the upper bound on $\tau \rightarrow 3\mu$ decay [10].

If we insist that the Fermi-LAT excess is due to the light h^\pm loop, then we get $\mu_{hk} \gtrsim 14$ TeV, which is inconsistent with the constraint $\mu_{hk} \lesssim 450$ GeV from the vacuum stability bound [9]. And there should be additional contributions to neutrino masses, such as from dim-5 Weinberg operators. If these dim-5 operators are induced through Type-I seesaw mechanism, the new physics would not affect our conclusion. On the other hand, if the dim-5 operators are induced by TeV scale seesaw, then the new physics from TeV scale seesaw might affect our conclusions.

Although it is not very satisfactory that the original Zee-Babu model with scalar dark matter cannot explain both the Fermi-LAT 130 GeV γ ray excess and neutrino physics simultaneously, it would be more natural to consider the Zee-Babu model as a low energy effective theory. Then it would be natural there could be new contributions to the neutrino masses and mixings from dim-5 operators. The only relevant question would be whether those new physics would affect the Fermi-LAT γ -ray or not. If the new physics is Type-I seesaw, there would be no new charged particles so that our conclusion would remain valid.

3 Spontaneously broken $U(1)_{B-L}$ model

As we have seen in the previous section, the simplest extension of Zee-Babu model to incorporate dark matter with Z_2 symmetry, although very predictive, has difficulty in fully explaining the Fermi-LAT gamma-line anomaly. In this section we consider a next minimal model where we may solve the problem. We further extend the model by introducing $U(1)_{B-L}$ symmetry and additional complex scalar φ to break the global symmetry [11, 12].

Then the model Lagrangian (2.3) is modified as

$$\begin{aligned}
-\mathcal{L}_{\text{Higgs+DM}} = & -\mu_H^2 H^\dagger H + \mu_X^2 X^* X + \mu_h^2 h^+ h^- + \mu_k^2 k^{++} k^{--} - \mu_\varphi^2 \varphi^* \varphi \\
& + (\mu_{\varphi X} \varphi X X + h.c.) \\
& + (\lambda_\mu \varphi h^- h^- k^{++} + h.c.) \\
& + \lambda_H (H^\dagger H)^2 + \lambda_\varphi (\varphi^* \varphi)^2 + \lambda_X (X^* X)^2 + \lambda_h (h^+ h^-)^2 + \lambda_k (k^{++} k^{--})^2 \\
& + \lambda_{H\varphi} H^\dagger H \varphi^* \varphi + \lambda_{HX} H^\dagger H X^* X + \lambda_{Hh} H^\dagger H h^+ h^- + \lambda_{Hk} H^\dagger H k^{++} k^{--} \\
& + \lambda_{\varphi X} \varphi^* \varphi X^* X + \lambda_{\varphi h} \varphi^* \varphi h^+ h^- + \lambda_{\varphi k} \varphi^* \varphi k^{++} k^{--} \\
& + \lambda_{Xh} X^* X h^+ h^- + \lambda_{Xk} X^* X k^{++} k^{--} + \lambda_{hk} h^+ h^- k^{++} k^{--}, \tag{3.1}
\end{aligned}$$

where we also replaced the real scalar dark matter X in (2.3) with the complex scalar field. The charge assignments of scalar fields are given as follows:

	H	h^+	k^{++}	φ	X
$U(1)_Y$	$\frac{1}{2}$	1	2	0	0
$U(1)_{B-L}$	0	2	2	2	-1

We note that the soft lepton number breaking term $\mu_{hk} h^+ h^+ k^{--}$ in (2.3) is now replaced by the $B-L$ preserving $\lambda_\mu \varphi h^+ h^+ k^{--}$ term. The $U(1)_{B-L}$ symmetry is spontaneously broken after φ obtains vacuum expectation value (vev). In [9], it was shown that $\mu_{hk} < \mathcal{O}(1) m_{h^+}$ to make the scalar potential stable. In this $U(1)_{B-L}$ model, this can be always guaranteed by taking small λ_μ , since $\mu_{hk} = \lambda_\mu v_\varphi$ even for very large v_φ . The term $\mu_{X\varphi} X X \varphi$ leaves Z_2 symmetry unbroken after $U(1)_{B-L}$ symmetry breaking. Under the remnant Z_2 symmetry, X is odd while all others are even. It appears that the theory is reduced to Z_2 model in (2.3) when φ is decoupled from the theory. But we will see that this is not the case and the effect of φ is not easily decoupled.

After H and φ fields get vev's, in the unitary gauge we can write

$$H = \begin{pmatrix} 0 \\ \frac{1}{\sqrt{2}}(v_H + h) \end{pmatrix}, \quad \varphi = \frac{1}{\sqrt{2}}(v_\varphi + \phi) e^{i\alpha/v_\varphi}, \tag{3.2}$$

where α is the Goldstone boson associated with the spontaneous breaking of global $U(1)_{B-L}$. For convenience we also rotated the field X

$$X \rightarrow X e^{-i\alpha/2v_\varphi} \tag{3.3}$$

so that the Goldstone boson does not appear in the $\mu_{\varphi X} \varphi X X$ term. Then the Goldstone boson interacts with X via the usual derivative coupling coming from the kinetic term of X -field.

The neutral scalar fields h and ϕ can mix with each other to give the mass eigenstates $H_i (i = 1, 2)$ by rotating

$$\begin{pmatrix} h \\ \phi \end{pmatrix} = \begin{pmatrix} c_H & s_H \\ -s_H & c_H \end{pmatrix} \begin{pmatrix} H_1 \\ H_2 \end{pmatrix}, \quad (3.4)$$

where $c_H \equiv \cos \alpha_H$, $s_H \equiv \sin \alpha_H$, with α_H mixing angle, and we take H_1 as the SM-like ‘‘Higgs’’ field. Then mass matrix can be written in terms of mass eigenvalues m_i^2 of $H_i (i = 1, 2)$:

$$\begin{pmatrix} 2\lambda_H v_H^2 & \lambda_{H\phi} v_H v_\phi \\ \lambda_{H\phi} v_H v_\phi & 2\lambda_\phi v_\phi^2 \end{pmatrix} = \begin{pmatrix} m_1^2 c_H^2 + m_2^2 s_H^2 & (m_2^2 - m_1^2) c_H s_H \\ (m_2^2 - m_1^2) c_H s_H & m_1^2 s_H^2 + m_2^2 c_H^2 \end{pmatrix} \quad (3.5)$$

where α_H is obtained from the relation

$$\tan 2\alpha_H = \frac{\lambda_{H\phi} v_H v_\phi}{\lambda_\phi v_\phi^2 - \lambda_H v_H^2}. \quad (3.6)$$

There is a mass splitting between the real and imaginary part of X :

$$X = \frac{X_R + iX_I}{\sqrt{2}}. \quad (3.7)$$

In the scalar potential we have 22 parameters in total. We can trade some of those parameters for masses,

$$\mu_X^2 = \frac{1}{2}(m_R^2 + m_I^2 - \lambda_{HX} v_H^2 - \lambda_{\phi X} v_\phi^2), \quad (3.8)$$

$$\mu_{\phi X} = \frac{m_R^2 - m_I^2}{2\sqrt{2}v_\phi}, \quad (3.9)$$

$$\mu_h^2 = m_{h^+}^2 - \frac{1}{2}\lambda_{Hh} v_H^2 - \frac{1}{2}\lambda_{\phi h} v_\phi^2, \quad (3.10)$$

$$\mu_k^2 = m_{k^{++}}^2 - \frac{1}{2}\lambda_{Hk} v_H^2 - \frac{1}{2}\lambda_{\phi k} v_\phi^2, \quad (3.11)$$

where $m_{R(I)}$ is the mass of $X_{R(I)}$. For simplicity we take X_R as the dark matter candidate from now on. We can also express $\lambda_H, \lambda_\phi, \lambda_{H\phi}$ in terms of masses $m_i^2 (i = 1, 2)$ and mixing angle α_H , then we take the 22 free parameters as

$$\begin{aligned} & v_H (\simeq 246 \text{ GeV}), \quad v_\phi, \quad m_1 (\simeq 125 \text{ GeV}), \quad m_2, \quad \alpha_H, \\ & m_R, \quad m_I, \quad m_{h^+}, \quad m_{k^{++}}, \\ & \lambda_\mu, \quad \lambda_h, \quad \lambda_k, \quad \lambda_X, \\ & \lambda_{Hh}, \quad \lambda_{Hk}, \quad \lambda_{HX}, \quad \lambda_{\phi X}, \quad \lambda_{\phi h}, \quad \lambda_{\phi k}, \quad \lambda_{Xh}, \quad \lambda_{Xk}, \quad \lambda_{hk}, \end{aligned} \quad (3.12)$$

where two values, v_H and m_1 , have been measured as written in the parentheses.

3.1 $X_R X_R \rightarrow \gamma\gamma$ and Fermi-LAT 130 GeV γ -ray excess in $U(1)_{B-L}$ model

In this section we will see that we can obtain dark matter annihilation cross section into two photons, $X_R X_R \rightarrow \gamma\gamma$, large enough to explain the Fermi-LAT 130 GeV γ -line excess. There are two mechanisms to enhance the annihilation cross section in this model: H_2 -resonance and large v_ϕ . In these cases, since the SM Higgs, H_1 , contribution is small for small mixing angle α_H , we consider only the contribution of H_2 assuming $\alpha_H = 0$ (or $H_2 = \phi$). Allowing nonvanishing α_H would only increase the allowed region of parameter space. Then we obtain the annihilation cross section times relative velocity for $X_R X_R \rightarrow \gamma\gamma$,

$$\sigma v_{\text{rel}}(X_R X_R \rightarrow \gamma\gamma) = \frac{\alpha_{\text{em}}^2}{32\pi^3 s} \left| \frac{(\sqrt{2}\mu_{\phi X} + \lambda_{\phi X} v_\phi) v_\phi}{s - m_\phi^2 + i m_\phi \Gamma_\phi} \sum_{i=h,k} Q_i^2 \lambda_{\phi i} [1 - \tau_i f(\tau_i)] + \sum_{i=h,k} Q_i^2 \lambda_{X i} [1 - \tau_i f(\tau_i)] \right|^2, \quad (3.13)$$

where Q_i is electric charge of $i (= h^+, k^{++})$, $\tau_i = 4m_i^2/s$ and Γ_ϕ is total decay width of ϕ . Since $v_{\text{rel}} \approx 10^{-3} \ll 1$, we can approximate $s = 4m_R^2/(1 - v_{\text{rel}}^2/4) \approx 4m_R^2$. When $\alpha_H = 0$, the $H_2 (= \phi)$ can decay into two Goldstone bosons (α) or into two photons with partial decay width

$$\Gamma(\phi \rightarrow \alpha\alpha) = \frac{m_\phi^3}{32\pi v_\phi^2}, \quad (3.14)$$

$$\Gamma(\phi \rightarrow X_{R(I)} X_{R(I)}) = \frac{(\pm\sqrt{2}\mu_{\phi X} + \lambda_{\phi X} v_\phi)^2}{32\pi m_\phi} \sqrt{1 - \frac{4m_{R(I)}^2}{m_\phi^2}}, \quad (3.15)$$

$$\Gamma(\phi \rightarrow h^+ h^- (k^{++} k^{--})) = \frac{(\lambda_{\phi h(k)} v_\phi)^2}{16\pi m_\phi} \sqrt{1 - \frac{4m_{h^+}^2}{m_\phi^2}}, \quad (3.16)$$

$$\Gamma(\phi \rightarrow \gamma\gamma) = \frac{\alpha_{\text{em}}^2 v_\phi^2}{64\pi^3 m_\phi} \left| \sum_{i=h,k} Q_i^2 \lambda_{\phi i} [1 - \tau_i f(\tau_i)] \right|^2. \quad (3.17)$$

Then the total decay width of ϕ is the sum:

$$\Gamma_\phi = \Gamma(\phi \rightarrow \alpha\alpha) + \Gamma(\phi \rightarrow X_{R(I)} X_{R(I)}) + \Gamma(\phi \rightarrow h^+ h^- (k^{++} k^{--})) + \Gamma(\phi \rightarrow \gamma\gamma). \quad (3.18)$$

As mentioned above, Fig. 6 shows the two enhancement mechanisms for $X_R X_R \rightarrow \gamma\gamma$: the left panel for the ϕ -resonance and the right panel for the large v_ϕ . For these plots we set the parameters: $m_R = 130$, $m_I = 2000$, $m_{h^+} = 300$, $m_{k^{++}} = 500$ (GeV), $\lambda_{\phi h} = \lambda_{\phi k} = 0.1$, $\lambda_{\phi X} = \lambda_{Xh} = \lambda_{Xk} = 0.01$, $v_\phi = 1000$ (GeV) for the left plot and $m_\phi = 600$ (GeV) for the right plot. We can obtain the large annihilation cross section required to explain Fermi-LAT gamma-line data either near the resonance, $m_\phi \approx 2m_R$ (left panel) or at large v_ϕ (right panel). These behaviors can be understood easily from (3.13). In either of these cases only the 1st term in (3.13) gives large enhancement. The slope on the right of the resonance

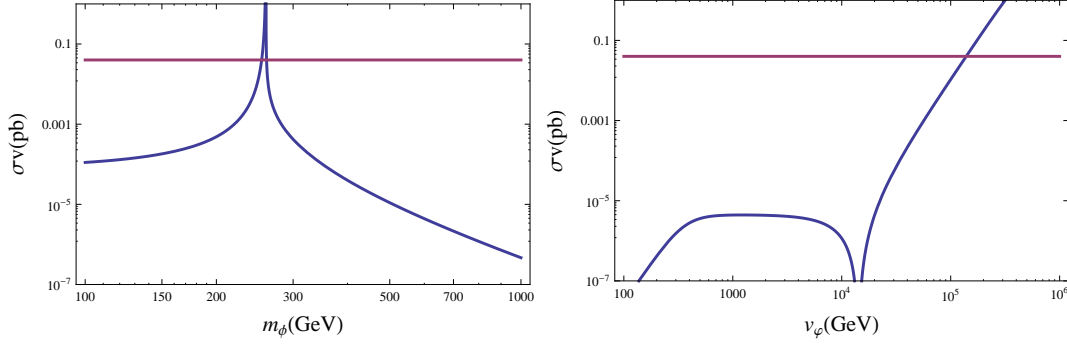


Figure 6. Plots of $\sigma v(X_R X_R \rightarrow \gamma\gamma)$ for $\alpha_H = 0$ as a function of $m_\phi (= m_2)$ (left panel) and v_ϕ (right panel). We set $m_R = 130$, $m_I = 2000$, $m_{h^+} = 300$, $m_{k^{++}} = 500$ (GeV), $\lambda_{\phi h} = \lambda_{\phi k} = 0.1$, $\lambda_{\phi X} = \lambda_{Xh} = \lambda_{Xk} = 0.01$, $v_\phi = 1000$ (GeV) for the left panel and $m_\phi = 600$ (GeV) for the right panel. The horizontal red line represent $\sigma v(X_R X_R \rightarrow \gamma\gamma) = 0.04$ (pb) which can explain the Fermi-LAT gamma-line signal.

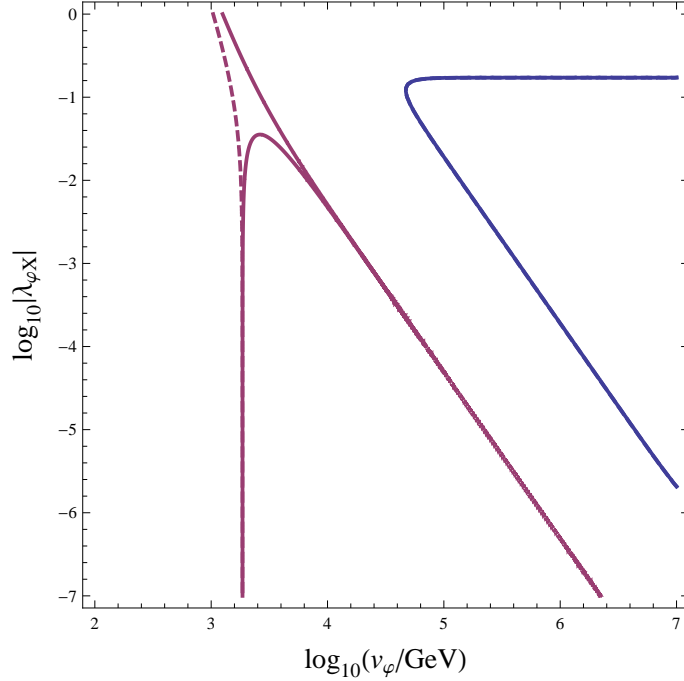


Figure 7. Contour plot of $\sigma v(X_R X_R \rightarrow \gamma\gamma) = 0.04$ (pb) in $(v_\phi, \lambda_{\phi X})$ -plane. The red lines represent the ϕ -resonance solution and the blue lines represent the large v_ϕ solution. The solid (dashed) lines are for positive (negative) $\lambda_{\phi X}$. See the text for the parameters chosen for this plot.

peak (the left panel of Fig. 6) is steeper than that on the left because, when $m_\phi > 260$ GeV, new annihilation channel $\phi \rightarrow X_R X_R$ opens and the decay width of ϕ increases leading to decreasing the annihilation cross section. In the right panel of Fig. 6, the dip near $v_\phi \approx 10^4$ GeV occurs because there is cancellation between $\sqrt{2}\mu_{\phi X} = (m_R^2 - m_I^2)/(2v_\phi)$ and $\lambda_{\phi X} v_\phi$ terms for positive $\lambda_{\phi X}$.

The two mechanisms can also be seen in Fig. 7. This figure shows a contour plot of $\sigma v(X_R X_R \rightarrow \gamma\gamma) = 0.04$ (pb) in $(v_\phi, \lambda_{\phi X})$ -plane. We set $m_R = 130$, $m_I = 1000$, $m_{h^+} = 1000$, $m_{k^{++}} = 1000$, $m_\phi = 260$ (GeV), $\lambda_{\phi h} = \lambda_{\phi k} = \lambda_{Xh} = \lambda_{Xk} = 0.01$ for red lines (ϕ -resonance). And we take $m_I = 1000$, $m_{h^+} = 300$, $m_{k^{++}} = 500$, $m_\phi = 600$ (GeV), $\lambda_{\phi h} = \lambda_{\phi k} = 0.1$, $\lambda_{Xh} = \lambda_{Xk} = 0.01$ for blue line (large v_ϕ). The red (blue) lines represent the ϕ -resonance (large v_ϕ) solution for Fermi-LAT anomaly. In the ϕ -resonance region, for the negative (positive) $\lambda_{\phi X}$ the two values $\sqrt{2}\mu_{\phi X} = (m_R^2 - m_I^2)/(2v_\phi)$ and $\lambda_{\phi X} v_\phi$ which appear in the 1st term of (3.13) have the same (opposite) sign and their contributions are constructive (destructive). As a result for positive $\lambda_{\phi X}$ (solid red line), there is cancellation between the two terms, and larger value of v_ϕ is required for a given $\lambda_{\phi X}$. For large v_ϕ case, the result does not depend on the sign of $\lambda_{\phi X}$ because the $\lambda_{\phi X} v_\phi$ term dominates. And the solid and dashed blue lines overlap each other in Fig. 7. For $\lambda_{\phi X}$ larger than about 0.1 the decay width $\Gamma(\phi \rightarrow X_R X_R)$ becomes too large to enhance the annihilation cross section.

3.2 Relic density in $U(1)_{B-L}$ model

Now we need to check whether the large enhancement in $X_R X_R \rightarrow \gamma\gamma$ signal is consistent with the observed relic density $\Omega_{\text{DM}} h^2 = 0.1199 \pm 0.0027$. To obtain the current relic density the DM annihilation cross section at decoupling time should be approximately (assuming S -wave annihilation)

$$\langle\sigma v\rangle_{\text{th}} \approx 3 \times 10^{-26} \text{ cm}^3/\text{s} \approx 1 \text{ pb}, \quad (3.19)$$

from (1.1). The major difference between the Z_2 model and the $U(1)_{B-L}$ model is that the latter model has additional annihilation channel, i.e., $X_R X_R \rightarrow \alpha\alpha$ and ϕ -exchange s -channel diagrams compared with the former one. The S -wave contribution to $\sigma v(X_R X_R \rightarrow \alpha\alpha)$ is shown in the Appendix. The Goldstone boson mode becomes dominant especially when v_ϕ is not very large [12], i.e. $v_\phi \lesssim 10^3$ GeV. And it makes the dark matter phenomenology very different from the one without it. For example, in Z_2 model we need the annihilation channel $XX \rightarrow h^+ h^- (k^{++} k^{--})$ large enough to obtain the current relic density. In $U(1)_{B-L}$ model, however, the annihilation into Goldstone bosons are sometimes large enough to explain the relic density.²

To see the relevant parameter space satisfying both the Fermi-LAT 130 GeV gamma-line anomaly and the correct relic density, we consider the ϕ -resonance and large v_ϕ cases discussed above separately. Fig. 8 shows contours of $\sigma v(X_R X_R \rightarrow \gamma\gamma) = 0.04$ (pb) (solid line) and $\Omega_{X_R} h^2 \approx 0.12$ (dashed line) for $\lambda_{\phi X} > 0$ when the resonance condition $m_\phi = 2m_R$ is satisfied. The parameters are chosen as $m_\phi = 2m_R = 260$ GeV, $m_I = m_{h^+} = m_{k^{++}} = 1$ TeV, $\lambda_{\phi h} = \lambda_{\phi k} = \lambda_{Xh} = \lambda_{Xk} = 0.01$. We can see there are intersection points of the two lines where both Fermi-LAT anomaly and the relic density can be explained. For the parameters we have chosen the contribution of $X_R X_R \rightarrow \alpha\alpha$ to the relic density is

²The dark sector can be in thermal equilibrium with the SM plasma in the early universe even with very small mixing $\alpha_H \sim 10^{-8}$ [13]. And our analysis with $\alpha_H = 0$ can be thought of as a good approximation of more realistic case of non-zero but small α_H .

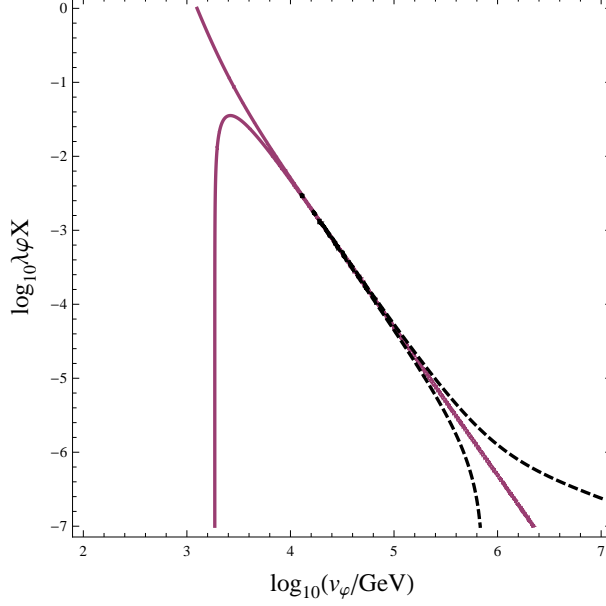


Figure 8. Contour plots of $\sigma v(X_R X_R \rightarrow \gamma\gamma) = 0.04$ pb (solid red line) and $\Omega_{DM} h^2 = 0.1199$ (dashed black line) in the $(v_\varphi, \lambda_{\varphi X})$ -plane for $\lambda_{\varphi X} > 0$. We take the parameters, $2m_R = m_\phi = 260$ GeV. See the text for other parameters. The region enclosed by the dashed lines gives $\Omega_{DM} h^2 > 0.12$.

almost 100%. This implies there is wide region of allowed parameter space satisfying both observables, since other annihilation channels $XX \rightarrow h^+ h^- (k^{++} k^{--})$ are also available when they are kinematically allowed. Typically TeV scalar v_φ gives too large $X_R X_R \rightarrow \alpha\alpha$ annihilation cross section resulting in too small relic density. For the positive $\lambda_{\varphi X}$ case, however, there is also cancellation between terms in $\sigma v(X_R X_R \rightarrow \alpha\alpha)$ as in $\sigma v(X_R X_R \rightarrow \gamma\gamma)$. Both cancellations are effective when the condition, $\lambda_{\varphi X} v_\varphi^2 = (m_I^2 - m_R^2)/2$, is satisfied. This explains the intersection point occurs on the diagonal straight line determined by the above condition. This allows large relic density even near TeV v_φ .

Fig. 9 shows the same contours for $\lambda_{\varphi X} < 0$. In this case as we have seen in Fig. 7 that TeV scale v_φ can explain Fermi-LAT gamma-line. However this value of v_φ gives too large DM annihilation cross section at the decoupling time (when $X_R X_R \rightarrow \alpha\alpha$ is dominant) and too small relic density. So somehow we need to “decouple” the $X_R X_R \rightarrow \gamma\gamma$ so that we need larger v_φ . We can do it, for example, by assuming $h^+(k^{++})$ are very heavy: $m_{h^+} = m_{k^{++}} = 5$ TeV. If we also reduce the mass difference $m_I - m_R$, we get smaller $\sqrt{2}\mu_{\varphi X} = -(m_I^2 - m_R^2)/(2v_\varphi)$. Then we have simultaneous solution both for $\sigma v(X_R X_R \rightarrow \gamma\gamma) \approx 0.04$ pb and $\Omega_{X_R} h^2 \approx 0.12$ as can be seen in Fig. 9. The two lines meet at rather large $v_\varphi (\sim 10^5$ GeV) as expected. For other parameters we chose³ $m_\phi \approx 2m_R = 260$ GeV, $m_I = 200$ GeV, $\lambda_{\varphi h} = \lambda_{\varphi k} = \lambda_{Xh} = \lambda_{Xk} = 0.01$. The pattern of the relic density contour requires some explanation. The annihilation cross section for $X_R X_R \rightarrow \alpha\alpha$ at the

³To avoid fine tuning we allowed small off-resonance condition of the size of $\Gamma_\phi \sim 1$ keV, *i.e.*, we set $m_\phi = 260.000001$ GeV.

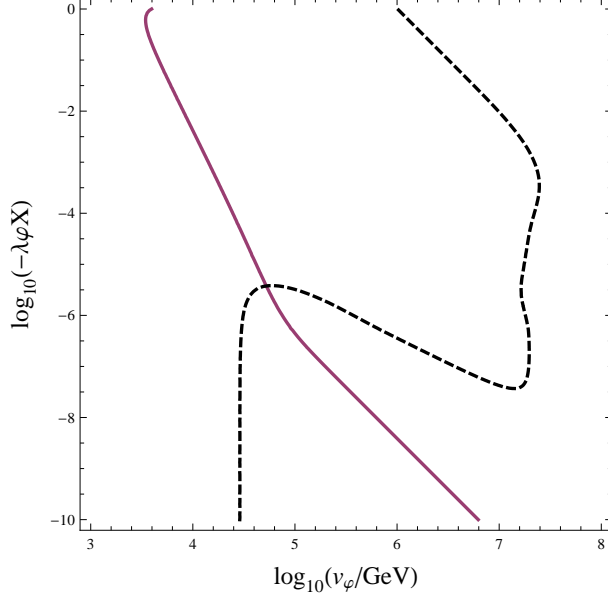


Figure 9. The same plot with Fig. 8 for $\lambda_{\phi X} < 0$. We also take the ϕ -resonance condition, $2m_R = m_\phi = 260$ GeV. See the text for other parameters. The region to the right of the dashed line gives $\Omega_{\text{DM}} h^2 > 0.12$.

resonance can be approximated from (B.1) as

$$\sigma v(X_R X_R \rightarrow \alpha\alpha) \approx \frac{(\sqrt{2}\mu_{\phi X} + \lambda_{\phi X} v_\phi)^2}{16\pi v_\phi^2 \Gamma_\phi^2}, \quad (3.20)$$

where Γ_ϕ is the total decay width of ϕ . The nonvanishing partial decay widths of ϕ for the parameters we chose are $\Gamma(\phi \rightarrow \alpha\alpha)$, $\Gamma(\phi \rightarrow X_R X_R)$ and $\Gamma(\phi \rightarrow \gamma\gamma)$. In Fig. 10 they are plotted as a function of v_ϕ for $\lambda_{\phi X} = -10^{-7}$. On the vertical part of the relic density contour in Fig. 9 near $v_\phi \sim 10^{4.4}$ GeV, the $\Gamma(\phi \rightarrow \alpha\alpha)$ dominates and also $\sqrt{2}\mu_{\phi X} \gg \lambda_{\phi X} v_\phi$. For this v_ϕ we approximately get

$$\sigma v(X_R X_R \rightarrow \alpha\alpha) \sim \frac{16\pi m_I^4}{m_\phi^6}, \quad (3.21)$$

which is independent of $\lambda_{\phi X}$. Around $v_\phi \sim 10^{7.2}$ GeV, $\Gamma(\phi \rightarrow X_R X_R)$ and $\Gamma(\phi \rightarrow \gamma\gamma)$ dominate despite high phase space suppression in $\phi \rightarrow X_R X_R$, and $\sqrt{2}\mu_{\phi X} \ll \lambda_{\phi X} v_\phi$. As $\lambda_{\phi X}$ increases, $\Gamma(\phi \rightarrow X_R X_R)$ becomes more important than $\Gamma(\phi \rightarrow \gamma\gamma)$ as can be seen from (3.14) and (3.15). The (almost) vertical part for this v_ϕ region is due to partial cancellation of the factor $(\sqrt{2}\mu_{\phi X} + \lambda_{\phi X} v_\phi)^2$ in the numerator of (3.20) and the same factor in the cross term of $\Gamma(\phi \rightarrow X_R X_R)$ and $\Gamma(\phi \rightarrow \gamma\gamma)$ in the denominator. As $\lambda_{\phi X}$ grows even larger, only $\Gamma(\phi \rightarrow X_R X_R)$ term dominates and $\sigma v(X_R X_R \rightarrow \alpha\alpha) \propto 1/\lambda_{\phi X}^2 v_\phi^4$, which gives the slanted part of the contour line.

We can also obtain simultaneous solutions when ϕ is off-resonance using large v_ϕ . Fig. 11 shows an example of this case. In this case, if we have only $X_R X_R \rightarrow \alpha\alpha$ -channel for relic density, the resulting $\Omega_{X_R} h^2$ is too large for $v_\phi \gtrsim 1$ TeV. To get the correct

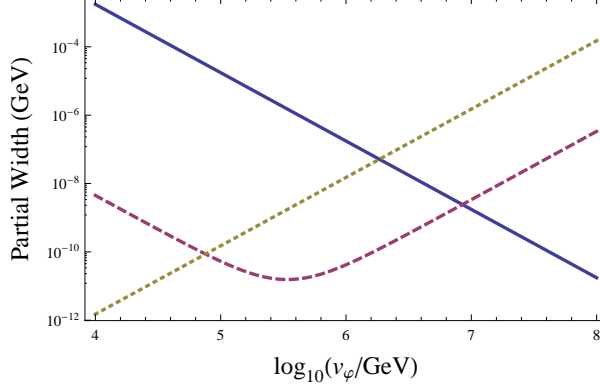


Figure 10. Plots of $\Gamma(\phi \rightarrow \alpha\alpha)$ (solid blue line), $\Gamma(\phi \rightarrow X_R X_R)$ (dashed red line) and $\Gamma(\phi \rightarrow \gamma\gamma)$ (dotted green line) as a function of v_ϕ for the parameters used in Fig. 9. We fixed $\lambda_{\phi X} = -10^{-7}$.

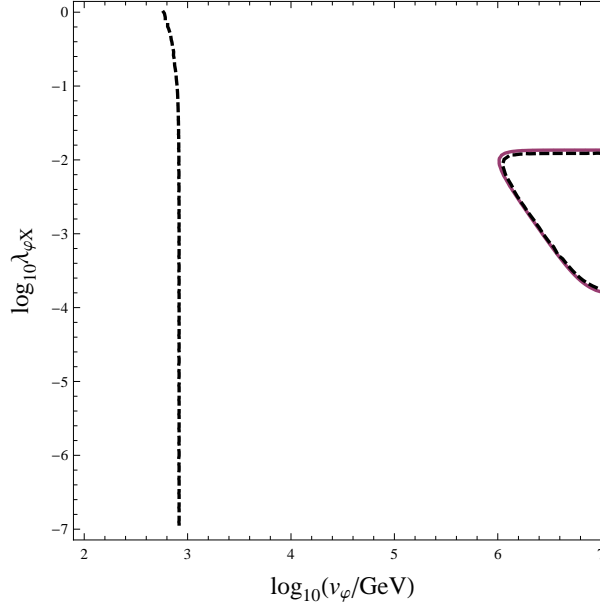


Figure 11. The same plot with Fig. 8 corresponding to large v_ϕ solution. See the text for the parameters used in this figure.

relic density by increasing the DM pair annihilation cross section at freeze-out we allowed $X_R X_R \rightarrow h^+ h^-$ channel. Then we can get a solution as can be seen in Fig. 11. The region enclosed by two dashed lines overcloses the universe. For this plot, we chose $m_R = 130$ GeV, $m_\phi = m_I = 1$ TeV, $m_{h^+} = 150$ GeV, $m_{k^{++}} = 500$ GeV, $\lambda_{\phi h} = 0.001$, and $\lambda_{\phi h} = \lambda_{\phi k} = \lambda_{Xh} = \lambda_{Xk} = 0.01$. Note that we take $\lambda_{\phi h} = 0.001$ so that the solid red line representing $\sigma v(X_R X_R \rightarrow \gamma\gamma) = 0.04$ pb and dashed line representing $\Omega h^2 = 0.1199$ overlap with each other. To show that this choice of λ 's is possible in general, we take a point on the overlapped lines, *e.g.*, $v_\phi = 10^{6.43}$ GeV and $\lambda_{\phi X} = 0.001$. Then we can get $\lambda_{\phi h} = 0.001, \lambda_{\phi k} = 0.01$ as a solution from Fig. 12.

When there is no mixing between ϕ and h the decay width $H_1 \rightarrow \gamma\gamma$ is the same with

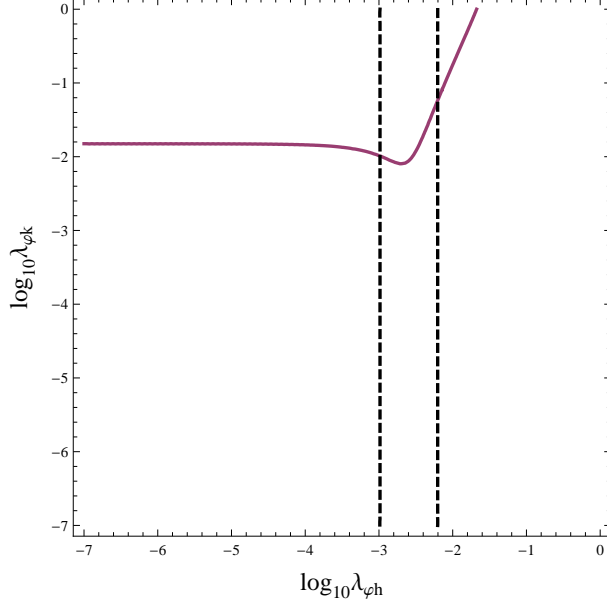


Figure 12. Contours of $\sigma v(X_R X_R \rightarrow \gamma\gamma) = 0.04$ pb (solid red line) and $\Omega h^2 = 0.1199$ (dashed blue line).

that of the SM. This means that we can enhance the $X_R X_R \rightarrow \gamma\gamma$ without affecting the SM $H_1 \rightarrow \gamma\gamma$ rate. When the mixing angle α_H is nonvanishing the h^+ and/or k^{++} can contribute to $H_1 \rightarrow \gamma\gamma$ through one-loop process. Since this effect was already discussed in Sec. 2.4, we do not discuss it further.

Weinberg [14] showed that Goldstone bosons can play the role of dark radiation and contribute to the effective number of neutrinos N_{eff} . When Goldstone bosons go out of equilibrium when the temperature is above the mass of muons and electrons but below that of all other SM particles, we get $\Delta N_{\text{eff}} = 0.39$. The condition for this to happen is [14]

$$\frac{\lambda_{H\varphi}^2 m_\mu^7 M_{\text{Pl}}}{m_\phi^4 m_H^4} \approx 1. \quad (3.22)$$

For example, with $\lambda_{H\varphi} = 0.005$ and $m_H = 125$ GeV, the dark scalar with mass 500 MeV can satisfy the condition.

4 Conclusions

We have considered two scenarios which minimally extended the ‘Zee-Babu model’ [7–9]. In the first scenario we introduced a real scalar dark matter X with Z_2 symmetry: $X \rightarrow -X$. If the scalar dark matter X has a mass around 130 GeV, the annihilation cross section, $\langle\sigma v\rangle(XX \rightarrow \gamma\gamma)$, can be enhanced by the contribution of the singly- and/or doubly-charged Zee-Babu scalars. If we also want to explain the dark matter relic abundance, however, we get at most $\langle\sigma v\rangle_{\gamma\gamma} \approx 0.2 \times 10^{-27} \text{cm}^3/\text{s}$, which is about factor 6 smaller than the required value to explain the Fermi-LAT gamma-ray line signal.

We have shown that the present constraint on the couplings λ_{Xk} and λ_{Xh} which mix the dark matter and charged Higgs is not so strong and they can enhance the annihilation cross section of $XX \rightarrow \gamma\gamma$ large enough to accommodate the recent hint. On the other hand the couplings which involve the SM Higgs H are strongly constrained by the theoretical considerations in the Higgs potential and the observations of dark matter relic density and dark matter direct detections. The upper bound on the λ_{HX} coupling is about 0.06 which comes from the dark matter direct detection experiments. For the $\lambda_{Hh}, \lambda_{Hk}$ which mix the SM Higgs and the new charged Higgs, the theoretical bound becomes more important. If we require the absolute stability of the dark matter by the Z_2 symmetry $X \rightarrow -X$ and the absence of charge breaking, we get the upper bound of $\lambda_{Hh}, \lambda_{Hk}$ to be about 0.7 for the charged Higgs mass around 150 GeV. To evade the unbounded-from-below Higgs potential we need to have $\lambda_{Hh}, \lambda_{Hk} \gtrsim -1.6$. With these constraints the $B(H \rightarrow \gamma(Z)\gamma)$ can be enhanced up to 1.5 (1.1) or suppressed down to 0.5 (0.9) with respect to that in the SM. The neutrino sector cannot be described by the Zee-Babu model only, and there should be additional contributions to the neutrino masses and mixings such as dimension-5 Weinberg operator from type-I seesaw mechanism.

In the second scenario, we introduced two complex scalar fields X and φ with global $U(1)_{B-L}$ symmetry. After φ gets vev, v_φ , the $U(1)_{B-L}$ symmetry is broken down to Z_2 symmetry. The lighter component of X , which we take to be the real part, X_R , is stable due to the remnant Z_2 symmetry and can be a dark matter candidate. Even in the extreme case where we do not consider the mixing of the dark scalar and the standard model Higgs scalar ($\alpha_H = 0$), we showed that the dark matter relic abundance and the Fermi-LAT gamma-ray line signal can be accommodated in two parameter regions: resonance region ($m_\phi = 2m_R$) and large $v_\varphi (\sim 10^6 - 10^7 \text{ GeV})$ region. Since there is no mixing, there is no correlation with $H \rightarrow \gamma\gamma$ and direct detection scattering of dark matter off the proton. In addition the neutrino sector need not be modified contrary to the first scenario.

Acknowledgments

This work is partly supported by NRF Research Grant 2012R1A2A1A01006053 (PK, SB).

A One-loop β functions of the quartic couplings

Here, we give the renormalization group equation and the one-loop β functions of the quartic couplings:

$$\frac{d\lambda_i}{d\ln Q} = \beta_{\lambda_i}, \quad (\text{A.1})$$

with

$$\beta_{\lambda_H} = \frac{1}{16\pi^2} \left[24\lambda_H^2 + \lambda_{Hh}^2 + \lambda_{Hk}^2 + \frac{\lambda_{HX}^2}{2} - 6y_t^4 + \frac{3}{8} \{ 2g_2^4 + (g_2^2 + g_1^2)^2 \} \right. \\ \left. - 4\lambda_H \left\{ \frac{3}{4}(3g_2^2 + g_1^2) - 3y_t^2 \right\} \right], \quad (\text{A.2})$$

$$\beta_{\lambda_h} = \frac{1}{16\pi^2} \left[16\lambda_h^2 + 2\lambda_{Hh}^2 + \lambda_{hk}^2 + \frac{\lambda_{Xh}^2}{2} + 6g_1^4 - 12\lambda_h g_1^2 \right], \quad (\text{A.3})$$

$$\beta_{\lambda_k} = \frac{1}{16\pi^2} \left[16\lambda_k^2 + 2\lambda_{Hk}^2 + \lambda_{hk}^2 + \frac{\lambda_{Xk}^2}{2} + 96g_1^4 - 48\lambda_k g_1^2 \right], \quad (\text{A.4})$$

$$\beta_{\lambda_X} = \frac{1}{16\pi^2} \left[18\lambda_X^2 + 2\lambda_{HX}^2 + \lambda_{Xh}^2 + \lambda_{Xk}^2 \right], \quad (\text{A.5})$$

$$\beta_{\lambda_{Hh}} = \frac{1}{16\pi^2} \left[12\lambda_H \lambda_{Hh} + 8\lambda_h \lambda_{Hh} + 2\lambda_{hk} \lambda_{Hh} + \lambda_{HX} \lambda_{Xh} + 3g_1^4 \right. \\ \left. - \lambda_{Hh} \left\{ \frac{3}{2}(3g_2^2 + g_1^2) - 6y_t^2 + 6g_1^2 \right\} \right], \quad (\text{A.6})$$

$$\beta_{\lambda_{Hk}} = \frac{1}{16\pi^2} \left[12\lambda_H \lambda_{Hk} + 8\lambda_k \lambda_{Hk} + 2\lambda_{hk} \lambda_{Hh} + \lambda_{HX} \lambda_{Xk} + 12g_1^4 \right. \\ \left. - \lambda_{Hk} \left\{ \frac{3}{2}(3g_2^2 + g_1^2) - 6y_t^2 + 24g_1^2 \right\} \right], \quad (\text{A.7})$$

$$\beta_{\lambda_{hk}} = \frac{1}{16\pi^2} \left[4\lambda_{Hh} \lambda_{Hk} + 8\lambda_{hk}(\lambda_h + \lambda_k) + \lambda_{Xh} \lambda_{Xk} + 48g_1^4 - 30\lambda_{hk} g_1^2 \right], \quad (\text{A.8})$$

$$\beta_{\lambda_{HX}} = \frac{1}{16\pi^2} \left[12\lambda_H \lambda_{HX} + 2\lambda_{Hh} \lambda_{Xh} + 2\lambda_{Hk} \lambda_{Xk} + 6\lambda_X \lambda_{HX} - \lambda_{HX} \left\{ \frac{3}{2}(3g_2^2 + g_1^2) - 6y_t^2 \right\} \right], \quad (\text{A.9})$$

$$\beta_{\lambda_{Xh}} = \frac{1}{16\pi^2} \left[4\lambda_{Hh} \lambda_{HX} + 8\lambda_h \lambda_{Xh} + 2\lambda_{hk} \lambda_{Xk} + 6\lambda_X \lambda_{Xh} - 6\lambda_{Xh} g_1^2 \right], \quad (\text{A.10})$$

$$\beta_{\lambda_{Xk}} = \frac{1}{16\pi^2} \left[4\lambda_{Hk} \lambda_{HX} + 8\lambda_k \lambda_{Xk} + 2\lambda_{hk} \lambda_{Xh} + 6\lambda_X \lambda_{Xk} - 24\lambda_{Xk} g_1^2 \right]. \quad (\text{A.11})$$

B The annihilation cross section of $X_R X_R \rightarrow \alpha\alpha$

The annihilation cross section of $X_R X_R \rightarrow \alpha\alpha$ is obtained as:

$$\sigma v(X_R X_R \rightarrow \alpha\alpha) = \frac{m_R^2 \left[4v_\varphi(\sqrt{2}\mu_{\varphi X} + \lambda_{\varphi X} v_\varphi)(m_I^2 + m_R^2) + (m_I^2 - m_R^2)(4m_R^2 - m_\phi^2) \right]^2}{64\pi v_\varphi^4 (m_I^2 + m_R^2)^2 (4m_R^2 - m_\phi^2)^2} \\ + O(v^2), \quad (\text{B.1})$$

where $(4m_R^2 - m_\phi^2)^2$ should be replaced by $(4m_R^2 - m_\phi^2)^2 + \Gamma_\phi^2 m_\phi^2$ in the denominator when $2m_R \approx m_\phi$.

References

- [1] P. A. R. Ade *et al.* [Planck Collaboration], arXiv:1303.5076 [astro-ph.CO].

- [2] Y. .B. Zeldovich, A. A. Klypin, M. Y. .Khlopov and V. M. Chechetkin, Sov. J. Nucl. Phys. **31**, 664 (1980) [Yad. Fiz. **31**, 1286 (1980)].
- [3] T. Bringmann, X. Huang, A. Ibarra, S. Vogl and C. Weniger, arXiv:1203.1312 [hep-ph].
- [4] C. Weniger, arXiv:1204.2797 [hep-ph].
- [5] E. Tempel, A. Hektor and M. Raidal, arXiv:1205.1045 [hep-ph]; E. Dudas, Y. Mambrini, S. Pokorski and A. Romagnoni, arXiv:1205.1520 [hep-ph]; J. M. Cline, arXiv:1205.2688 [hep-ph]; K. -Y. Choi and O. Seto, Phys. Rev. D **86**, 043515 (2012) [arXiv:1205.3276 [hep-ph]]; B. Kyae and J. -C. Park, arXiv:1205.4151 [hep-ph]; H. M. Lee, M. Park and W. -I. Park, arXiv:1205.4675 [hep-ph]; B. S. Acharya, G. Kane, P. Kumar, R. Lu and B. Zheng, arXiv:1205.5789 [hep-ph]; M. R. Buckley and D. Hooper, Phys. Rev. D **86**, 043524 (2012) [arXiv:1205.6811 [hep-ph]]; X. Chu, T. Hambye, T. Scarna and M. H. G. Tytgat, arXiv:1206.2279 [hep-ph]; D. Das, U. Ellwanger and P. Mitropoulos, JCAP **1208**, 003 (2012) [arXiv:1206.2639 [hep-ph]]; D. Das, U. Ellwanger and P. Mitropoulos, JCAP **1208**, 003 (2012) [arXiv:1206.2639 [hep-ph]]; Z. Kang, T. Li, J. Li and Y. Liu, arXiv:1206.2863 [hep-ph]; N. Weiner and I. Yavin, arXiv:1206.2910 [hep-ph]; L. Feng, Q. Yuan and Y. -Z. Fan, arXiv:1206.4758 [astro-ph.HE]; W. Buchmuller and M. Garny, JCAP **1208**, 035 (2012) [arXiv:1206.7056 [hep-ph]]; J. H. Heo and C. S. Kim, arXiv:1207.1341 [astro-ph.HE]; E. Hardy, J. March-Russell and J. Unwin, arXiv:1207.1435 [hep-ph]; M. T. Frandsen, U. Haisch, F. Kahlhoefer, P. Mertsch and K. Schmidt-Hoberg, arXiv:1207.3971 [hep-ph]; J. -C. Park and S. C. Park, arXiv:1207.4981 [hep-ph]; S. Tulin, H. -B. Yu and K. M. Zurek, arXiv:1208.0009 [hep-ph]; T. Li, J. A. Maxin, D. V. Nanopoulos and J. W. Walker, arXiv:1208.1999 [hep-ph]; J. M. Cline, A. R. Frey and G. D. Moore, arXiv:1208.2685 [hep-ph]; Y. Bai and J. Shelton, arXiv:1208.4100 [hep-ph]; R. Laha, K. C. Y. Ng, B. Dasgupta and S. Horiuchi, arXiv:1208.5488 [astro-ph.CO]; L. Bergstrom, arXiv:1208.6082 [hep-ph]; L. Wang and X. -F. Han, arXiv:1209.0376 [hep-ph]; S. Baek and H. Okada, Phys. Lett. B **728**, 630 (2014) [arXiv:1311.2380 [hep-ph]].
- [6] J. M. Cline, in Ref. [5]
- [7] A. Zee, Nucl. Phys. B **264**, 99 (1986).
- [8] K. S. Babu, Phys. Lett. B **203**, 132 (1988).
- [9] K. S. Babu and C. Macesanu, Phys. Rev. D **67**, 073010 (2003) [hep-ph/0212058].
- [10] D. Aristizabal Sierra and M. Hirsch, JHEP **0612**, 052 (2006) [hep-ph/0609307].
- [11] D. Chang, W. -Y. Keung and P. B. Pal, Phys. Rev. Lett. **61**, 2420 (1988).
- [12] M. Lindner, D. Schmidt and T. Schwetz, Phys. Lett. B **705**, 324 (2011) [arXiv:1105.4626 [hep-ph]].
- [13] S. Baek, P. Ko, W. -I. Park and Y. Tang, arXiv:1402.2115 [hep-ph].
- [14] S. Weinberg, Phys. Rev. Lett. **110**, 241301 (2013) [arXiv:1305.1971 [astro-ph.CO]].
- [15] S. Chatrchyan *et al.* [CMS Collaboration], Phys. Lett. B **710**, 26 (2012) [arXiv:1202.1488 [hep-ex]].
- [16] S. Chatrchyan *et al.* [CMS Collaboration], arXiv:1207.2666 [hep-ex].
- [17] D. S. Akerib *et al.* [LUX Collaboration], arXiv:1310.8214 [astro-ph.CO].
- [18] J. Beringer *et al.* [Particle Data Group Collaboration], Phys. Rev. D **86**, 010001 (2012).